

Journal of the Atmospheric Sciences

New statistical model for variability of aerosol optical thickness: Theory and application to MODIS data over ocean --Manuscript Draft--

Manuscript Number:	JAS-D-15-0130
Full Title:	New statistical model for variability of aerosol optical thickness: Theory and application to MODIS data over ocean
Article Type:	Article
Corresponding Author:	Mikhail Alexandrov Columbia University New York, UNITED STATES
Corresponding Author's Institution:	Columbia University
First Author:	Mikhail Alexandrov
Order of Authors:	Mikhail Alexandrov
	Igor Geogdzhayev
	Kostas Tsigaridis
	Alexander Marshak
	Robert Levy
	Brian Cairns
Abstract:	<p>A novel model for the variability in aerosol optical thickness (AOT) is presented. This model is based on the consideration of AOT fields as realizations of a stochastic process, that is the exponent of an underlying Gaussian process with a specific autocorrelation function. In this approach AOT fields have lognormal PDFs and structure functions having the correct asymptotic behavior at large scales. The latter is an advantage compared with fractal (scale-invariant) approaches. The simple analytical form of the structure function in the proposed model facilitates its use for the parameterization of AOT statistics derived from remote sensing data. The new approach is illustrated using a month-long global MODIS AOT dataset (over ocean) with 10 km resolution. It was used to compute AOT statistics for sample cells forming a grid with 5° spacing. The observed shapes of the structure functions indicated that in a large number of cases the AOT variability is split into two regimes that exhibit different patterns of behavior: small-scale stationary processes and trends reflecting variations at larger scales. The small-scale patterns are suggested to be generated by local aerosols within the marine boundary layer, while the large-scale trends are indicative of elevated aerosols transported from remote continental sources. This assumption is evaluated by comparison of the geographical distributions of these patterns derived from MODIS data with those obtained from the GISS GCM. This study shows considerable potential to enhance comparisons between remote sensing datasets and climate models beyond regional mean AOTs.</p>

and Application to MODIS Data over Ocean

Mikhail D. Alexandrov ^{*} and Igor V. Geogdzhayev

Department of Applied Physics and Applied Mathematics, Columbia University,
and NASA Goddard Institute for Space Studies, New York, New York

Kostas Tsigaridis

*Center for Climate Systems Research, Columbia University,
and NASA Goddard Institute for Space Studies, New York, New York*

Alexander Marshak and Robert Levy

NASA Goddard Space Flight Center, Greenbelt, Maryland

Brian Cairns

NASA Goddard Institute for Space Studies, New York, New York

*Corresponding author address: Mikhail D. Alexandrov, NASA Goddard Institute for Space Studies, 2880 Broadway, New York, NY 10025.

E-mail: mda14@columbia.edu

ABSTRACT

16 A novel model for the variability in aerosol optical thickness (AOT) is pre-
17 sented. This model is based on the consideration of AOT fields as realizations
18 of a stochastic process, that is the exponent of an underlying Gaussian pro-
19 cess with a specific autocorrelation function. In this approach AOT fields have
20 lognormal PDFs and structure functions having the correct asymptotic behav-
21 ior at large scales. The latter is an advantage compared with fractal (scale-
22 invariant) approaches. The simple analytical form of the structure function in
23 the proposed model facilitates its use for the parameterization of AOT statis-
24 tics derived from remote sensing data. The new approach is illustrated using a
25 month-long global MODIS AOT dataset (over ocean) with 10 km resolution.
26 It was used to compute AOT statistics for sample cells forming a grid with
27 5° spacing. The observed shapes of the structure functions indicated that in a
28 large number of cases the AOT variability is split into two regimes that exhibit
29 different patterns of behavior: small-scale stationary processes and trends re-
30 flecting variations at larger scales. The small-scale patterns are suggested to
31 be generated by local aerosols within the marine boundary layer, while the
32 large-scale trends are indicative of elevated aerosols transported from remote
33 continental sources. This assumption is evaluated by comparison of the geo-
34 graphical distributions of these patterns derived from MODIS data with those
35 obtained from the GISS GCM. This study shows considerable potential to
36 enhance comparisons between remote sensing datasets and climate models
37 beyond regional mean AOTs.

38 1. Introduction

39 Atmospheric aerosols through their direct and indirect radiative effects remain a significant
40 source of uncertainty for the historical forcing of climate (Hansen et al. 2000; Myhre et al. 2013;
41 Koch et al. 2007; Unger et al. 2008) and consequently for the assessment of projected change.
42 Resolving this uncertainty requires the synergistic combination (through inter-comparisons and
43 assimilations) of aerosol models and observational datasets (Kinne et al. 2006; Quaas et al. 2009;
44 Huneus et al. 2011). As a part of an effort to define new strategies and methodologies for the
45 inter-comparison of model and satellite data it looks promising to include analysis of more de-
46 tailed characteristics of aerosol variability and go beyond traditional comparison of aerosol optical
47 thickness (AOT) averaged over a geographical region. In particular, structure functions (SFs)
48 provide a uniform description of the strength and spatial scale of AOT fluctuations. The structure
49 function (see e.g., Davis et al. (1994) and the next section) describes the average difference in value
50 over scale. In the framework of traditional scale-invariant (fractal) models the SF is assumed to
51 have a power-law form characterized by the scaling (Hurst) exponent H . SFs together with power
52 spectra have been widely used to characterize scaling of turbulence-driven fluctuations of various
53 atmospheric fields, such as temperature, wind speed, humidity, etc. (e.g., Gage and Nastrom 1986;
54 Lilly 1989; Lovejoy and Schertzer 2010, 2012). Scaling techniques were also successfully used
55 in analysis of various cloud datasets (Cahalan and Snider 1989; Davis et al. 1996, 1997, 1999;
56 Marshak et al. 1997).

57 The scaling properties of AOT were studied by Anderson et al. (2003) using autocorrelation
58 statistics. This study revealed that mesoscale aerosol variability (at 40 – 400 km scales) is a com-
59 mon feature of lower-tropospheric aerosol light extinction. Another application of scaling analysis
60 to AOT variability was performed by Alexandrov et al. (2004). They studied AOT scaling using

the 1-month dataset from a sun-photometers network operated by the U.S. Department of Energy Atmospheric Radiation Measurement program in Oklahoma and Kansas. The network provided an irregular grid with the mean distance between neighboring sites of roughly 80 km and temporally the sampling was 20 s. This data set therefore allowed for both temporal and spatial AOT variability to be analyzed. Alexandrov et al. (2004) found that the temporal variability of AOT can be separated into two scale-invariant regimes: microscale (0.5 – 15 km) where fluctuations are governed by 3D turbulence ($H \approx 0.3$); and intermediate scale (15 – 100 km) characterized by a transition towards large-scale 2D turbulence ($H \approx 0.4 - 0.5$). The temporal evolution of AOT scaling exponents during the month appeared to be correlated with changes in aerosol vertical distribution, while their spatial variability reflected the site’s topography.

Unfortunately, the scale-invariant variability model with its power-law SF being divergent at large scales does not naturally reflect an important statistical property of real AOT fields: the statistical independence of AOT values at points separated by a large distance. This property means that the SF approaches a constant value (double the AOT variance) at a sufficiently large scale. To deal with this problem within the fractal framework a number of scaling regimes are introduced separated by scale breaks. In this study we present a new AOT variability model that has an advantage over the scale-invariant approach because its SFs have the correct asymptotic behavior. In this approach we construct an AOT field by taking the exponent of an underlying Gaussian random process with specified autocorrelation function. This ensures that AOT fields have lognormal PDFs (O’Neill et al. 2000), while their structure functions are power-law at small scales and approach a constant at large scales. The simple analytical expression for the SF of this model facilitates its application to real AOT datasets.

We will apply our analytical model to the statistics derived from global Moderate Resolution Imaging Spectroradiometer (MODIS) AOT product (Remer et al. 2005, 2008; Levy et al. 2010).

85 It will be shown that the shapes of the MODIS-derived SFs in many cases suggest the presence of
86 two distinctive variability modes, which we attribute to two aerosol layers separated by height (one
87 within the boundary layer, the other above it). Such a separation adds a “third dimension” to the
88 2D MODIS dataset, and can be quantitatively evaluated by comparison with the aerosol vertical
89 structure in climate models (even if the climate model resolution is insufficient for computation of
90 the SFs themselves). To demonstrate this possibility, we present a comparison between the aerosol
91 modes derived from the MODIS dataset and those obtained using 3D AOT fields simulated by the
92 NASA Goddard Institute for Space Studies (GISS) General Circulation Model (GCM) ModelE2
93 (Schmidt et al. 2014).

94 **2. Statistics of AOT fields**

95 Statistical properties of AOT (as well as of many other geophysical parameters) are characterized
96 by their probability distribution (PDF) and structure functions (SF). The latter describes the de-
97 pendence of the expected difference between AOT values measured at two points in space or time
98 on their separation (see e.g., Davis et al. (1994); Alexandrov et al. (2004); Lovejoy and Schertzer
99 (2012)). The SF is equivalent to the variogram that is used in geostatistics (Curran 1988). In our
100 model we will use the second-order SF that is defined for a 1D case as follows

$$\begin{aligned}
 S_2(r) &= \overline{[\tau(x+r) - \tau(x)]^2} \\
 &= \frac{1}{L-r} \int_0^{L-r} [\tau(x+r) - \tau(x)]^2 dx.
 \end{aligned}
 \tag{1}$$

101 Here τ is the AOT, r is the lag, or separation between points, and the over-bar denotes averaging
102 over $x \in [0, L]$, where L is the sample size. This implies the validity of the ergodicity hypothesis
103 such that an ensemble average over realizations is equivalent to an average over the spatial variable

104 x . The definition of S_2 is equivalent to that of the variance of the increment field

$$\Delta_r \tau(x) = \tau(x+r) - \tau(x), \quad (2)$$

105 i.e.

$$S_2(r) = \text{Var}(\Delta_r \tau), \quad (3)$$

106 assuming that $\overline{\Delta_r \tau} = 0$. The structure function definition for the 2D case is similar to that for the
107 1D case:

$$S_2(r) = \overline{[\tau(\mathbf{x} + \mathbf{r}) - \tau(\mathbf{x})]^2}, \quad (4)$$

108 where \mathbf{x} and \mathbf{r} are now 2D vectors, and $r = |\mathbf{r}|$. The averaging in \mathbf{x} is performed over some spatial
109 domain. This implicitly assumes statistical isotropy of the AOT field.

110 Computation of a structure function (1D or 2D) does not require continuity of the AOT dataset,
111 which can have gaps or even be a collection of values at discrete points in space or time. To derive
112 a SF we take all available data points and consider all possible pairs of them. For each pair we
113 calculate the distance and the difference in AOT between the two points. Then the set of these
114 distances and differences from all pairs is used to build a histogram (square difference in AOT vs.
115 distance between points), which is the SF for this dataset.

116 If the aerosol field consists of n independent (e.g., separated by height) layers each having an
117 AOT of $\tau^{(i)}(x)$, the total AOT

$$\tau(x) = \sum_{i=1}^n \tau^{(i)}(x) \quad (5)$$

118 will have the following statistics:

$$\bar{\tau} = \sum_{i=1}^n \overline{\tau^{(i)}}, \quad \text{Var}(\tau) = \sum_{i=1}^n \text{Var}(\tau^{(i)}), \quad (6)$$

119 and

$$S_2(\tau; r) = \sum_{i=1}^n S_2(\tau^{(i)}; r). \quad (7)$$

120 The latter relation follows from Eq. (3).

121 In the important case of scale-invariant (fractal) fields structure functions have a power-law form:

$$S_2(r) \propto r^{2H}, \quad (8)$$

122 where $H \in (0,1)$ is the Hurst exponent (Mandelbrot 1982). Larger values of H correspond to
123 smoother functions that may have substantial trends, while smaller values indicate finer scale vari-
124 ability and more stationarity (see e.g., Marshak et al. (1997)). A Hurst exponent of 1/2 corresponds
125 to classical Brownian motion (CBM), which is a Markov process with independent increments.
126 Processes with other values of H , called fractional Brownian motions (FBM), are non-Markovian:
127 their increments either correlate (for $H > 1/2$), or anti-correlate (for $H < 1/2$). The theoretical
128 values of H that are characteristic of variability in wind speed and passive scalar advection in tur-
129 bulent flows are 1/3 for 3D turbulence (Kolmogorov 1941), and 1 for 2D turbulence (e.g., Gage
130 and Nastrom 1986). In their study of sun-photometer-derived AOT time series Alexandrov et al.
131 (2004) found values of H ranging from 0.1 to 0.6.

132 It is known that AOT fields exhibit a scale-invariant structure over certain scale ranges (Alexan-
133 drov et al. 2004), however, AOT variability at all scales cannot be described by a single fractal
134 model. It is natural to assume that the AOT values at two points located far enough from each
135 other can be considered independent. Thus, at large scales $S_2(r)$ becomes the variance of the dif-
136 ference between two independent variables, which is equal to the sum of the variances of those
137 variables. As we assume that the AOT field is statistically homogeneous, these variances are the
138 same and equal to the global variance of the dataset. Thus,

$$S_2(r \rightarrow \infty) \simeq 2 \text{Var}(\tau), \quad (9)$$

139 is a scale-independent constant. A power-law SF Eq. (8), which diverges at large scales, is incon-
 140 sistent with this asymptotic constraint (i.e., the global variance does not exist in fractal models).
 141 This means that fractal characterization of AOT variability can be made only over a restricted range
 142 of scales, and the value of the exponent H will be dependent on the range of scales selected. In a
 143 model with finite global mean $\bar{\tau}$ and variance $\text{Var}(\tau) = s^2$ the autocorrelation function is defined
 144 to be

$$W(r) = \frac{[\tau(x) - \bar{\tau}][\tau(x+r) - \bar{\tau}]}{\text{Var}(\tau)}, \quad (10)$$

145 which is related to the structure function by the expression

$$S_2(r) = 2s^2[1 - W(r)]. \quad (11)$$

146 The asymptotic condition Eq. (9) then means that $W \rightarrow 0$ as $r \rightarrow \infty$.

147 **3. The statistical model for AOT**

148 In this Section we will define the AOT variability model and derive the corresponding expres-
 149 sions for structure and autocorrelation functions. AOT datasets are known to have lognormal PDFs
 150 (O'Neill et al. 2000) and it is therefore natural to use a statistical model of them where $\tau = \exp(\eta)$,
 151 with η being a Gaussian field defined by its mean, variance, and autocorrelation function $w(r)$.
 152 Realizations of such a process can be constructed using Fourier filtering techniques that use power
 153 spectrum computed for a prescribed autocorrelation function (see e.g., Bell (1987)). An alterna-
 154 tive method to generate a Gaussian field using the summation of multiple realizations of a binary
 155 Markov process is described in the supplemental material.

156 It is shown in Appendix A following the approach described by Mejia and Rodriguez-Iturbe
 157 (1974) that the structure and autocorrelation functions of the AOT field can be expressed through

158 the autocorrelation function $w(r)$ of the underlying Gaussian process:

$$S_2(r) = 2s^2 \frac{u - u^{w(r)}}{u - 1}, \quad (12)$$

159

$$W(r) = \frac{u^{w(r)} - 1}{u - 1}. \quad (13)$$

160 Here we use the notation

$$u = \frac{s^2 + \bar{\tau}^2}{\bar{\tau}^2}, \quad (14)$$

161 where $\bar{\tau}$ and s are respectively the mean and standard deviation of the AOT field. The function
 162 $w(r)$ should be positive and obey the following properties: $w(0) = 1$ and $w(r \rightarrow \infty) = 0$. The
 163 former insures that $S_2(0) = 0$, while the latter means that $S_2(r \rightarrow \infty) = 2s^2$. Probably, the simplest
 164 functional form of $w(r)$ satisfying these conditions is exponential:

$$w_M(r) = e^{-r/L_e}, \quad (15)$$

165 where L_e is the autocorrelation length. For example, the autocorrelation function of the Gaussian
 166 model based on binary Markov processes (see the supplemental material) has this form. When
 167 $w(r)$ is exponential, the structure function is linear in the small-scale limit: $S_2(r \ll L_e) \propto r$. This
 168 is appropriate for an AOT field that behaves as a classical Brownian motion (having the Hurst
 169 exponent $H = 1/2$). However, in our previous study (Alexandrov et al. 2004) that considered
 170 relatively small temporal and spatial scales we found that the AOT's structure functions showed
 171 power-law dependence on the lag: $S_2(r \ll L_e) \propto r^{2H}$. We will see similar small-scale behavior
 172 of SFs computed for the MODIS AOT product. This means that at small scales real AOT fields
 173 resemble FBMs with Hurst exponents not necessarily equal to 1/2. These observations prompt us
 174 to generalize the exponential functional shape in Eq. (15) to accomodate the appropriate power
 175 law behavior for the small-scale limit case. We choose the following expression:

$$w(r) = e^{-(r/L_e)^{2H}}, \quad (16)$$

176 which is analytically simple and captures the observed behavior of real AOT fields. For non-
 177 exponential $w(r)$ parameter L_e is not precisely the autocorrelation length, so we will call it the
 178 “characteristic length” instead. It characterizes the typical size of inhomogeneities in the AOT
 179 field. Figure 1 shows how the shape of the reduced structure function $S_2(r)/2s^2$ computed accord-
 180 ing to Eqs. (12) and (16) depends on the three parameters: the relative standard deviation $v = s/\bar{\tau}$,
 181 L_e , and H . We see that the dependence on v is relatively weak, while variations in L_e change the
 182 length scale of the function. It is also seen that the SF’s value at $r = L_e$ does not depend on H (this
 183 simplifies fitting of remote sensing data).

184 **4. Derivation of the model parameters from observations**

185 We assume that the observational dataset provides a PDF of AOT values (from which we deter-
 186 mine the mean $\bar{\tau}$ and the standard deviation s), as well as the structure function $S_2(r)$. Then, we
 187 compute the parameter u according to Eq. (14) and derive the formula

$$w(r) = \frac{1}{\ln u} \ln \left[u - \frac{u-1}{2s^2} S_2(r) \right] \quad (17)$$

188 from Eq. (12). After this, the model parameters can be obtained from Eq. (16) when it is written
 189 as

$$-\ln w(r) = \left(\frac{r}{L_e} \right)^{2H}. \quad (18)$$

190 First, we determine L_e from the condition

$$-\ln w(L_e) = 1. \quad (19)$$

191 The small-scale Hurst exponent H can then be derived from Eq. (18) by linear regression in
 192 $\ln(r/L_e)$:

$$\ln[-\ln w(r)] = 2H \ln \left(\frac{r}{L_e} \right). \quad (20)$$

5. Application to the MODIS AOT product

The proposed variability model was evaluated using the AOT product (collection 5 level 2, 550 nm wavelength) from the MODIS instrument on the Terra satellite (Levy et al. 2010). MODIS is on polar-orbit, observing a 2330 km-wide swath. There are gaps in MODIS observations near the equator, while the measurements from different orbits overlap near the poles. The aerosol retrieval creates a “10 km” product, which has 10 km resolution at nadir, extending to 40 km at swath edge. We took a one-year-long (2006) global AOT dataset with 10 km resolution and computed the means, variances, and structure functions for the data from overlapping $10^\circ \times 10^\circ$ cells (with ocean and land treated separately). The centers of the cells form a grid with $5^\circ \times 5^\circ$ resolution. In order to avoid the effects of overlapping orbits on the satellite data at high latitudes we restricted our retrievals to the area between 60°S and 60°N . Here we present the results of our analysis only for the measurements over ocean, where variability of surface albedo is small compared to that of AOT.

Computation of structure functions follows the procedure outlined in Section 2. For a given day and a given $10^\circ \times 10^\circ$ cell we take all available 10×10 km pixels. If the number of these pixels exceeds a threshold of two hundred regardless of their distribution within the cell, we proceed with the analysis and consider all possible pairs of pixels. For each pair of pixels we determine the distance and the difference in AOT between them. After this we collect these parameters from all pairs and use them to construct a histogram of square difference in AOT vs. distance between pixels using a 10 km bin size. This histogram is regarded as the SF for this cell. Note that the computation of SFs for 2D datasets implies statistical isotropy, thus, the resulting structure function is the directionally averaged representation of AOT variability. We estimate the mean and the standard deviation of the AOT in the cell using the data from the available pixels and use these

values to parameterize the SF according to our model, as described in Section 4. This procedure, applied to all admissible cells, provides a global daily dataset of $\bar{\tau}$, s , and the SF parameters L_e and H on a grid with 5° resolution (our $10^\circ \times 10^\circ$ cells overlap). Combining these parameter values over multiple days gives us a time series, which we average over a month (using only the days when the data are available) to obtain the monthly mean values. The averaging helps to reduce the statistical noise in the dataset. It appears that the above described parameterization does not always provide a good fit to the observed SF due to insufficient sample size (see Section 6 for details). While the SF parameters still have a qualitative meaning in such cases, we modify our analysis (as described in Section 7) to better explore the information content of the data.

6. Sampling effects

It is generally difficult to characterize the accuracy of structure functions computed from satellite data, since in each case we have to deal with a single realization of the stochastic process governing the variability in the AOT. The statistics computed using this realization may deviate from those of the (hypothetical) complete statistical ensemble, so we have to assume that this deviation is not significant. Using multiple datasets does not solve this problem since the AOT variability parameters are not the same for different times, locations, and sample sizes. The size of the sample ($10^\circ \times 10^\circ$ in our case) is a free parameter to be chosen by the investigator. It should be large enough to collect enough satellite pixels for statistical analysis, while still sufficiently small to reveal spatial variability in the derived statistics. Another issue with the SF analysis, as well as with any statistical method applied to satellite data, is whether the AOT values at the pixels where retrievals are available are representative of the whole sample area. This is of particular concern if the number of available pixels is small or their spatial distribution is uneven. Note that over ocean, less than 10% of all global 10 km boxes in the MODIS product have valid AOT retrieval due to

239 avoidance of clouds and sunglint. We deal with this issue by setting a threshold on the number of
240 data pixels in the sample, and also by controlling the quality of SFs (those that are too noisy to be
241 well fit by our models are discarded).

242 To give an example of the effect of sample size on the retrieved statistical parameters we compare
243 structure functions and their parameterizations from two datasets representative of different scales
244 (shown in Fig. 2). One of these areas is a $120^\circ \times 70^\circ$ region covering more than half of the Pacific
245 Ocean, while the other is its local subset – a typical $10^\circ \times 10^\circ$ cell used in our analysis. The data are
246 from January 17, 2006. The top left panel of Fig. 3 shows the regional structure function (the AOT
247 data used for the SF computation is shown in the insert). We see that 5000 km scale is sufficient
248 to observe the beginning of the SF’s saturation. The AOT in this sample has a mean of 0.13 and a
249 standard deviation of 0.062. Despite some noise at larger scales this SF fits our variability model
250 well with $L_e = 815$ km and $H = 0.39$. The top right panel of Fig. 3 shows the same SF (red curve)
251 over a smaller lag range (up to 1500 km) together with the SF from the $10^\circ \times 10^\circ$ subset (green
252 curve). We see that while the local SF largely inherits the shape of the regional one, the 1000 km
253 sampling range is not sufficient to reach the scale at which the SF saturates. Note also that the
254 the local standard deviation of 0.042 is 30% smaller than that for the large region. The bottom
255 panels of Fig. 3 demonstrate that the local SF can be fit by our model in different ways depending
256 on whether the local (bottom left) or regional (bottom right) variance value is used yielding very
257 different values of L_e : respectively 165 and 845 km.

258 A qualitative analysis of the influence of the number of pixels on the computation of the SF
259 is presented in Fig. 4. This plot shows the complete local SF from Fig. 3 (green curve) and the
260 number N_p of pixel pairs contributing to this SF at each scale (black curve). This number increases
261 with the lag at small scales, while decreasing at large scales due to the effect of finite sample size.
262 It looks like the effect of N_p on the SF starts to dominate once a threshold is crossed. The SF

monotonically increases with lag and is in good agreement with its regional analog (Fig. 3 (top right)) up to the scale of 1100 km (dashed line in Fig. 4), at which point it “breaks”. The number of pairs at this lag is 1800. The reason for this behavior is in the rapid growth at this point of $N_p^{-1/2}$, which determines the statistical uncertainty of the SF computation. This is illustrated in Fig. 4 by two orange curves corresponding to $S_2 \pm \text{const} \cdot N_p^{-1/2}$ (the constant here is taken equal to $2 \max(S_2)$). The admissible scale range with a number of pairs larger than this value is shown in Fig. 4 by the blue horizontal line. Besides the part with $r > 1100$ km, this range does not include the first two bins corresponding to lags of less than 20 km. We will see below that such a scale range is sufficient for SF parameterization.

The example described above demonstrates that there are two negative effects of having a smaller sample size on SFs and their parameterizations. First, the reduction in the number of pixel pairs especially affects the large-scale range, where the structure function is expected to saturate to its asymptotic value. This may yield “incomplete” SFs showing no saturation at all. Second, the dependence of the AOT variance on the sample size (when this size is small) may lead to ambiguity in parameterization of SFs.

7. Information content of “incomplete” structure functions

While the example from the previous section shows that an “incomplete” (not reaching saturation) structure function cannot be used for the retrieval of regional-scale statistics, such SFs can still provide valuable information on AOT variability at specific geographic locations. A closer look at the top right panel of Fig. 3 reveals a feature in the local SF curve at scales smaller than 600 km distinguishing it from the regional SF. We call this feature a “partial saturation”. The bottom left panel of Fig. 3 demonstrates that the shape of the local SF in this scale range is consistent with our model and using of the local variance in the fitting process. The fit yields $H = 0.56$ and

$L_e = 165$ km. This behavior can be explained by the presence of trends in small samples. These trends reflect the non-stationary nature of AOT variability at small scales (where it behaves as a FBM) and are averaged out in statistics for a sufficiently large dataset. To explain the shape of the partial saturation feature we decompose (using e.g., linear regression) the 1D or 2D small-scale AOT sample into a sum of two independent components: a trend (which is close to a linear function) and a stationary field. Then, according to Eq. (7), the total SF can be represented as a sum of SFs of these components. By the nature of this decomposition the stationary component's SF quickly saturates at scales smaller than the typical trend length. The structure function of the trend component has the form $S_2(r) \propto r^2$ (corresponding to fractal model with $H = 1$). The plot of a sum of such two functions (see Fig. 5) is similar to those in Figs. 3 and 6. Here we see a partial saturation at smaller scales (inherited from the stationary SF) followed by an increase at larger scales where the trend's SF starts to dominate. This pattern does not affect scales larger than the typical length of a trend.

The “strength” of a trend can be evaluated by the difference between the AOT variance in the sample and the stationary component variance inferred from the saturation value of its SF. For example, we see that the trend contributions to the SFs in Figs. 3 (bottom left) and 6 (a) are weak since in these cases the AOT variances in the samples can be explained by the stationary components alone. On the other hand, the SFs from Fig. 6 (b-e) show indications of stronger trends.

While some trends can be present in an ambient aerosol layer (as is likely to be the case in Fig. 3), stronger trends may indicate the presence of aerosol plumes transported above the marine boundary layer (MBL) from remote continental sources. Such plumes are large in scale and relatively “smooth” since they are not affected by boundary-layer turbulence. They are also localized (being a “plume”) by proximity to their sources and characteristic wind patterns. This localization

induces trends in AOT between the center of the plume and its edges. This allows us to assume a two-mode aerosol structure with a transported mode located above the MBL and associated with the trend component in AOT, and a local (or MBL) mode located within the MBL and associated with the stationary component in AOT.

The parameters of the transported mode SF cannot be retrieved using the local AOT variance, however, the MBL mode SF can be separated and characterized fairly well due to its small-scale saturation (see Appendix B for a description of the technique). Knowing the mean and the variance of the MBL AOT allows us to also determine the parameters of the transported mode by subtraction of the MBL values from those of the total SF.

Besides the two-mode method, we also continue to employ the single-mode technique described in Section 4. It uses the local variance and derives the values of L_e and H . While the quality of the fit of the SF to a single-mode model may be less than perfect, the characteristic lengths L_e obtained in this way still provide a proxy for the scale of total (not just MBL) AOT variability.

8. Examples of structure functions from MODIS dataset

Figure 6 presents examples of the structure functions computed using MODIS data from 5 different $10^\circ \times 10^\circ$ ocean regions (shown in the top left panel). All the data are from the same day, August 18, 2006, and the pixels used are shown in the inserts. In three out of five of the presented cases SFs show pronounced partial saturation at scales below 400 km indicative of strong trends in AOT. One of the exceptions is the case from the relatively pristine Pacific Ocean that is unaffected by long-range aerosol transport (Fig. 6(a), similar to bottom left panel of Fig. 3). The absence of a trend contribution to the AOT variance and the short characteristic length of the MBL component ($L_e = 65$ km) suggest that the aerosol in this area is predominantly from local sources, e.g., sea spray. The SF from African coastal waters (Fig. 6(b)) looks quite different. A large AOT value

(1.0) and partial saturation in the SF are consistent with significant amounts of Saharan dust in this region. There the aerosol has essentially a 2-layer structure with a lower local aerosol (e.g., sea spray) within the marine boundary layer (which typically has a height of 500 – 600 m) and an elevated dust layer transported from continental sources at 2 – 5 km above the sea level. If we assume that $\tau \propto s$ then two thirds of AOT in this case comes from the elevated layer. The single-mode estimate of the variability scale is large ($L_e = 475$ km), while the MBL component's SF has a much more modest scale $L_e = 115$ km. Besides locally produced sea spray, the MBL can also contain some dust falling from the elevated layer. Figure 6(c) presents the SF from an area off the coast of equatorial Africa that is known to be affected by biomass burning smoke from the continent. While this is quite an interesting region to study, the data look consistently noisier than those from other places. The relatively large ratio $s/\bar{\tau} = 0.75$ indicates intermittency (presence of isolated high values) in the sample, and may point to undetected clouds below the smoke layer. Some inconsistency between MODIS and CALIOP AOT from this region and season was also reported by Redemann et al. (2012). The plot in 6(d) shows the SF from the northern Indian Ocean off the coast of the Somali Peninsula. This area is affected by dust transport from the Arabian Peninsula. This structure function looks similar to that for the Saharan dust case (Fig. 6(b)) and has similar parameters, however, the AOT here is much smaller: 0.4. The SF from the middle of the Indian Ocean (Fig. 6(e)) also has a pronounced partial saturation feature, while the AOT ≈ 0.1 there is as small as in the Pacific Ocean case. This may indicate the presence of a rather thin elevated aerosol layer transported by the West winds (which are strong in this area in Summer) from the southern part of Africa.

9. Geographical mapping of AOT variability

The parameters of the structure functions derived from the MODIS global satellite dataset together with the means and variances of the AOT can be used to characterize aerosol variability on a planetary scale. We illustrate this possibility by constructing $5^\circ \times 5^\circ$ resolution maps of the AOT variability parameters averaged over the month of August 2006. Figure 7 presents maps of the mean AOT, its standard deviation, and the ratio of the standard deviation to the mean. It is interesting to observe that this ratio lacks features associated with high AOT areas (such as Saharan dust or biomass burning smoke), and the whole range of $s/\bar{\tau}$ variability is quite narrow: between 0.3 and 0.6.

The SF parameters L_e and H derived using the single-mode approach are presented in Fig. 8. The larger values of both of these parameters, especially L_e , correspond to the areas where continental aerosols are advected over the ocean: Saharan dust to the West of northern Africa and biomass burning smoke to the West of the sub-equatorial part of this continent, dust from the Arabian Peninsula spreading into the northern Indian Ocean, and also smoke and pollution transport from South America, Africa, and Australia driven by the westerly winds of the Southern Ocean (especially in the southern Indian Ocean). Except for the latter case, these areas are associated with large AOT values (see Fig. 7 (top)). One can observe an unusual low-value feature in the plot of H going in a South – North direction in the western Pacific, close to the international dateline. This artifact is probably caused by a known minor problem with the definition of the MODIS day (sometimes an orbit crossing the dateline is counted on the wrong day) and can also be seen in some other datasets (see e.g., Redemann et al. (2012)).

Under certain assumptions (described in Section 7 and in Appendix B) the structure function parameterization allows us to split the total AOT into the elevated (transported) and the MBL

377 modes. While the structure function of the elevated mode cannot be reliably characterized, the
378 MBL component's SF can be extracted and fitted by our model. The typical values of L_e for this
379 component are around 100 km and show little geographical structure, while the exponent H varies
380 between 0.2 and 0.5 with some decrease towards the Southern Ocean. In some cases (such as
381 the one presented in Fig. 6(a)) only one mode is detected in the SF. In our computations of the
382 averages we attribute such a single-mode AOT to the elevated mode if $L_e > 150$ km, and to the
383 MBL mode otherwise. The geographical distributions of the AOT components will be discussed
384 in Section 10 in comparison with GCM output.

385 **10. Comparison with GCM output**

386 While producing a plausible qualitative picture, the proposed layer separation technique needs
387 to be evaluated by comparison with 3D aerosol datasets. We obtained such dataset from the NASA
388 Goddard Institute for Space Studies (GISS) general circulation model (GCM) simulations for the
389 same month of August 2006 used in examples of MODIS data described above. GISS ModelE2
390 (Schmidt et al. 2014) produces 3D AOT fields with 2° resolution in latitude and 2.5° in longitude.
391 Vertical resolution of the model is defined in sigma units so it varies with surface pressure. Con-
392 verted to a height it is about 200 m at sea level and increases with altitude. The simulated AOT is
393 divided between several aerosol species: dust, sea salt, biomass burning, industrial pollution, and
394 secondary organic aerosols. Calculation of the boundary layer height in the model is based on the
395 “Richardson number criterion” as described by Yao and Cheng (2012).

396 The monthly averaged mean AOT map from the GCM simulations is presented in Fig. 9 (top).
397 Visual comparison between this map and that in Fig. 7 (top) reveals a number of qualitative
398 deviations of the model results from the observations including a notable lack of Saharan dust, a
399 smaller AOT in the Caribbean, and the presence of a large plume off the coast of Peru that is not

400 seen in the MODIS data. The largest model-satellite differences are seen in the Southern Ocean,
401 which is known to be one of the most difficult regions on the planet for both observations and
402 modeling. There the GCM-produced AOT values are as high as 0.3 – 0.4, while MODIS detects
403 only background aerosols with an optical thickness of 0.1 or less. These discrepancies in AOT
404 can be caused by many factors, detailed analysis of which is outside the scope of this study. For
405 example, the satellite retrievals can be affected by inadequate cloud screening, while the AOT in
406 the GCM may be biased by an anomalously large MBL height in the Southern Ocean (clearly seen
407 in Fig. 9 (bottom)), as well as by uncertainties in the assumed size distributions and hygroscopic
408 properties of sea salt aerosols.

409 Figure 10 presents the partition of the total AOT into the above-MBL (top) and within-MBL
410 (bottom) components. The plots on the left show the results from MODIS SF analysis, while the
411 right panels present the AOTs obtained from the partition of the GCM AOT profiles by the MBL
412 height (Fig. 9 (bottom)). Note that the MODIS-derived maps in Fig. 10 were “enhanced” to make
413 them look similar to the GCM plots: MODIS AOT was interpolated from the original $5^\circ \times 5^\circ$ grid
414 (as in Fig. 7), to the $2.5^\circ \times 2.5^\circ$ grid (similar to that of the model) and then smoothed using a
415 moving average. The larger model-satellite differences in the component optical thicknesses are
416 seen in the same regions as those in the total AOTs, e.g., in the Southern Ocean (where the model
417 attributes most of the AOT to the MBL component). As to the mode separation in general, we
418 see that in the regions with long-range transport of large aerosol masses (Saharan dust, biomass
419 burning in the western Africa) the SF analysis of the MODIS data has more aerosol in the boundary
420 layer than the model.

421 The partition of the AOT into two modes allows us to compute the fraction of the total AOT that
422 is in the elevated mode. This parameter can be used as an indicator of long-range transport, even
423 when the transported aerosol mass is optically thin. Fig. 11 presents the geographical distributions

of this ratio derived from the observations (left) and from the GCM data (right). Above, we mentioned that mixing between aerosol layers in the model is weaker than in the SF analysis. This means that the GCM AOT ratio plot has more contrast than its MODIS analog: large AOT ratios are larger, while the small ones are smaller. Thus, in order to facilitate comparisons between aerosol transport features in the model and observations and to make the corresponding maps more similar, we increased the contrast in Fig. 11 (left) by reducing the color range.

The geographical distribution of the AOT ratio in Fig. 11 (left) is similar to that of L_e in the single-mode approach that is shown in Fig. 8 (top). This confirms that large-scale features in AOT are associated with elevated plumes. In addition to the West African biomass burning and the dust advected from the Sahara and the Arabian Peninsula, the two panels of Fig. 11 show a number of more subtle similarities that are not readily seen in the total AOT plots. One of these transport features is the plume off the coast of Peru and Ecuador. The GCM classifies this plume as a combination of biomass burning and secondary organic aerosols, while it can also include some dust advected from the coastal Sechura Desert. Another common case is a smaller plume off the other coast of South America in the vicinity of Sao Paulo, Brazil. In the model this is identified as secondary organic aerosol, however the location of the plume also suggests that there may be contributions from Brazilian forest fire smoke transported by North-West winds and pollution from the Sao Paulo industrial area. The advection of industrial pollution (and, at lesser extent, biomass burning) from the eastern coast of South Africa across the Indian Ocean is more strongly pronounced in observational data than in the GCM results, although it is present in both datasets. The same can be said about the feature off the north-western coast of Australia having very small AOT (less than 0.1), which is probably associated with smoke. We should note, however, that the quality of the aerosol mode separation at such small AOTs may be questionable because of the limited accuracy of MODIS retrievals (cf. Levy et al. 2010). The largest differences between the

GCM results and our retrievals are seen in the Pacific. While our interpretation of MODIS data indicates long-range transport in the South Pacific by the westerly winds, the model, as can be seen in Fig. 10, attributes most of the aerosol there to the boundary layer. In the North Pacific the situation is opposite: the model shows transport from North America (especially northern Mexico), while we see no indication of this in the satellite data. We also see less transport from the US East Coast than is suggested by the model.

11. Conclusions

We introduced a new statistical model for variability of atmospheric AOT. It is based on a representation of AOT fields as realizations of a stochastic process, that is the exponent of an underlying Gaussian process with an autocorrelation function of the form given in Eq. (16). The AOT in this model has a lognormal PDF with the mean $\bar{\tau}$ and the standard deviation s , while its structure function has the analytical form defined by Eq. (12) with two parameters: the characteristic length L_e and the scaling exponent H . The AOT fields obeying our model formulation are similar to a fractional Brownian walk with the Hurst exponent H at small scales ($r \ll L_e$), while become stationary at large scales ($r \gg L_e$). This behavior is reflected in the shape of the SF: it has a power-law form at small lags r , while approaching a constant in the large-scale limit. This constant is equal to double the AOT's variance indicating, as expected, that AOT values from distant points are statistically independent. This asymptotic behavior of the SF gives our model an advantage compared to the traditional fractal (scale-invariant) model, in which the structure function has a power-law form at any scale, thus, diverging in the asymptotic regime. In the fractal framework, variability description for a realistic field often requires an artificial split of the scale range into several parts equipped with different fractal models and separated by scale breaks.

470 The simple analytical form of the SF in our model facilitates its use for parameterization of
 471 AOT statistics derived from remote sensing data. We gave examples of such applications using
 472 the MODIS AOT product (over ocean) at 10 km spatial resolution. We demonstrated using the
 473 data from $120^\circ \times 70^\circ$ area in Pacific Ocean that our statistical model adequately describes AOT
 474 variability on a regional scale with SF saturation occurring around 5000 km lag (Fig. 3 (top left)).
 475 We also computed the means, standard deviations, and SFs of the AOT field for a one-month-long
 476 global dataset consisting of overlapping $10^\circ \times 10^\circ$ sample cells, centers of which form a grid with
 477 5° spacing. Examples of SFs from a variety of such samples are presented in Fig. 6. While
 478 $10^\circ \times 10^\circ$ or higher grid resolution is necessary to capture geographical differences in the vari-
 479 ability patterns of AOT, this sample size appears to be too small for saturation of the SF to be
 480 observed. This together with scaling of the AOT's variance prevents us from performing a com-
 481 plete parameterization of these structure functions over the whole available scale range. However,
 482 some important information on AOT variability can still be obtained from these SFs based on their
 483 behavior at scales below 400 km, where they often exhibit partial saturation. This feature is in-
 484 dicative of a split in variability between non-stationary trends and stationary components that we
 485 attribute to local processes. The partial SF describing the stationary component saturates at scales
 486 around 100 km, so it can be extracted and parameterized according to our model. The presence of
 487 a strong trend in the data (that may be associated with long-range transport) can be detected even
 488 qualitatively, simply by looking at the shape of the SF. In such a case the variance corresponding to
 489 the partial saturation value of the SF is significantly smaller than the total variance in the sample.

490 While, rigorously speaking, we only observe the split in the total column AOT variability rather
 491 than that in aerosol mass, we can formally associate the large- and small-scale variability patterns
 492 with two aerosol modes each having its own fraction of the total AOT. One of these modes cor-
 493 responds to locally produced aerosol located within the marine boundary layer, while the other

494 represents non-local aerosol processes, such as long-range transport above the MBL. Geograph-
495 ical mapping of the results presented in Figs. 8 and 10 – 11 confirmed that areas where larger
496 values of characteristic lengths and higher fraction of elevated mode AOT are observed are also
497 known to be affected by long-range aerosol transport (desert dust, biomass burning smoke, etc.).
498 The advantage of our method is in its ability to detect transport of relatively thin aerosol plumes
499 that are not clearly identified in the total AOT datasets.

500 The set of variability parameters that can be derived from satellite data in addition to the
501 mean AOT has the potential to enhance comparisons between remote sensing datasets and cli-
502 mate models. High spatial resolution models can now provide data for structure function analy-
503 sis. Our preliminary tests showed that the $1.125^\circ \times 1.125^\circ$ resolution of the European Centre for
504 Medium-Range Weather Forecasts (ECMWF) model (Morcrette et al. 2009; Benedetti et al. 2009)
505 or the Spectral Radiation-Transport Model for Aerosol Species (SPRINTARS) (Takemura et al.
506 2000, 2005; Geogdzhayev et al. 2014) is sufficient for the computation of structure functions for
507 $10^\circ \times 10^\circ$ samples. However, even when a climate model does not have such high spatial resolu-
508 tion, it can still be used to calculate the elevated mode fraction in AOT, which is comparable to
509 that obtained from SF analysis of satellite data. Indeed, the 3D AOT from a climate model can be
510 divided using the boundary layer height into the MBL and elevated components. In this study we
511 presented a qualitative example of such a comparison between AOT mode separation results from
512 MODIS SF analysis and from the GISS GCM simulations. Despite some differences described in
513 Section 10, both datasets showed many similar aerosol transport patterns. Such comparisons are
514 very useful for further development and testing of the SF technique, and also for evaluating and im-
515 proving the models, especially in terms of their long-range transport and aerosol lifetime. We plan
516 to continue such comparisons in the future, also involving aerosol height resolved measurements
517 such as these made by Cloud-Aerosol LIdar with Orthogonal Polarization (CALIOP) onboard of

518 NASA Cloud-Aerosol Lidar and Infrared Pathfinder Satellite Observations (CALIPSO) satellite
 519 (Winker et al. 2009, 2010).

520 *Acknowledgment.* This research was funded by the NASA Radiation Sciences Program managed
 521 by Hal Maring. Kostas Tsigaridis acknowledges support from NASAs Atmospheric Composition
 522 Modeling and Analysis Program (ACMAP), contract number NNX15AE36G. Resources support-
 523 ing this work were provided by the NASA High-End Computing (HEC) Program through the
 524 NASA Center for Climate Simulation (NCCS) at Goddard Space Flight Center. We would like
 525 to thank the two anonymous reviewers for thoughtful remarks that allowed us to substantially
 526 improve the paper. We also thank A. Davis and M. Mishchenko for useful discussions.

527 APPENDIX A

528 Statistics of modelled AOT fields

529 Here we derive the statistics of the exponential AOT field

$$\tau = e^{\eta}. \quad (\text{A1})$$

530 based on a Gaussian process η having the mean μ , variance σ^2 , and autocorrelation function $w(r)$.

531 The field τ has log-normal PDF with the mean

$$\bar{\tau} = e^{\mu + \sigma^2/2} \quad (\text{A2})$$

532 and the variance

$$s^2 = (e^{\sigma^2} - 1) \bar{\tau}^2 = (u - 1) \bar{\tau}^2. \quad (\text{A3})$$

533 Here we introduced the parameter

$$u = e^{\sigma^2} = \frac{s^2 + \bar{\tau}^2}{\bar{\tau}^2}. \quad (\text{A4})$$

534 We start derivation of the structure function for τ with computation of the corresponding autocor-
 535 relation function. The covariance between $\tau_1 = \tau(t)$ and $\tau_2 = \tau(t+r)$ has the form

$$\text{Cov}(\tau_1, \tau_2) = \overline{(\tau_1 - \bar{\tau})(\tau_2 - \bar{\tau})} = \overline{\tau_1 \tau_2} - \bar{\tau}^2. \quad (\text{A5})$$

536 To compute it we need to know the mean of $\tau_1 \tau_2 = \exp(\eta_1 + \eta_2)$. The random variable $\eta_1 + \eta_2$
 537 being a sum of normally distributed variables is normally distributed itself. It has the mean 2μ and
 538 the variance

$$\begin{aligned} \text{Var}(\eta_1 + \eta_2) &= 2\text{Var}(\eta) + 2\text{Cov}(\eta_1 + \eta_2) \\ &= 2\sigma^2[1 + w(r)]. \end{aligned} \quad (\text{A6})$$

539 Thus, the exponent of this variable is distributed log-normally with the mean

$$\overline{\tau_2 \tau_1} = e^{2\mu + \sigma^2(1+w)} = \bar{\tau}^2 u^w. \quad (\text{A7})$$

540 Thus, the autocorrelation function for τ has the form

$$W(r) = \frac{\bar{\tau}^2(u^{w(r)} - 1)}{s^2} = \frac{u^{w(r)} - 1}{u - 1}. \quad (\text{A8})$$

541 Note that as $w(0) = 1$ and $w(r \rightarrow \infty) = 0$, $W(r)$ has the same properties. The structure function
 542 can be computed according to Eq. (11):

$$S_2(r) = 2s^2 \frac{u - u^{w(r)}}{u - 1} = 2s^2 \frac{u}{u - 1} (1 - u^{-z(r)}), \quad (\text{A9})$$

543 where $z(r) = 1 - w(r)$. It is easy to see that $S(0) = 0$ and $S_2(r \rightarrow \infty) = 2s^2$. In the small-scale
 544 limit, if we assume $z(r) \propto r^{2H}$, the structure function has the same power-law behavior:

$$S_2(r \rightarrow 0) \propto r^{2H}, \quad (\text{A10})$$

545 indicating that AOT behaves as Fractional Brownian motion with the Hurst exponent H .

Fitting structure functions with partial saturation

The real satellite data examples presented in Fig. 6 indicate that in many cases the structure function shapes deviate from the form described by Eqs. (12), (16), and Fig. 1. The characteristic concave feature in the 100–500 km scale range (partial saturation) suggest that these SFs are superpositions of two components corresponding to trend(s) and a relatively stationary AOT field. While the trend component’s SF is expected to be simply quadratic in scale, it appears that we can successfully fit the measured structure function using the same model for both components. This means that we formally assume that aerosol consists of two independent modes or layers. We need to keep in mind, however, that while the MBL SF has physical meaning, the representation of the trend contribution as a formal SF is an abstraction used only for fitting. Since parameters of the “trend SF” have no real meaning, we relax the requirement of $H < 1$ for it to improve fitting flexibility.

We assume that the stationary and the trend components are statistically independent as if they indeed correspond to two layers separated by height. Then the statistics of these components satisfy the system of equations following from Eqs. (5 – 7):

$$S_2(r) = S_2^{(1)}(r) + S_2^{(2)}(r), \quad (\text{B1})$$

$$\tau = \tau_1 + \tau_2, \quad (\text{B2})$$

$$s^2 = s_1^2 + s_2^2, \quad (\text{B3})$$

where τ , s , and $S_2(r)$ are known, while τ_1 , τ_2 , s_1 , s_2 , and the parameters of the two SF components are to be determined. Here and below index “1” corresponds to the trend component, while index “2” corresponds to the MBL component. The retrieval algorithm is essentially a curve fitting of the measured $S_2(r)$ by the family of component SFs with parameters satisfying the conditions Eqs.

(B2) and (B3). In order to make this fitting more robust, and to reduce the number of retrieved parameters (which may have trade-offs between them), we complement the latter two equations with another condition:

$$\frac{s_1}{\tau_1} = \frac{s_2}{\tau_2} \quad (\text{B4})$$

(which is equivalent to $u_1 = u_2$). We see in real satellite data shown in Fig. 7 that the ratio s/τ indeed is not very variable, so the assumption of Eq. (B4) is quite natural. In our approach first the single-mode retrieval is performed to get an estimate L_e of the variability scale. Then, the fitting is performed over a single free parameter $\alpha \in [0, 1]$, which is the fraction of the trend component in the total variance. In this notation

$$s_1 = s\sqrt{\alpha}, \text{ and } s_2 = s\sqrt{1-\alpha}, \quad (\text{B5})$$

and the retrieval method utilizes the assumption that the MBL component's structure function $S^{(2)}(r)$ quickly saturates and is close to the constant $2s_2^2$ in the scale range between $L_e/2$ and L_e . Thus, for each value of α the trend SF in this range can be computed as

$$S_2^{(1)}(r) = S_2(r) - 2s_2^2 = S_2(r) - 2s^2(1-\alpha). \quad (\text{B6})$$

This SF is then fitted in the range $[L_e/2, L_e]$ according to the method described in Section 4, given

$$\begin{aligned} u_1 &= \frac{s_1^2}{\tau_1^2} + 1 = \frac{(s_1 + s_2)^2}{\tau^2} + 1 \\ &= (\sqrt{\alpha} + \sqrt{1-\alpha})^2 \frac{s^2}{\tau^2} + 1. \end{aligned} \quad (\text{B7})$$

Here we used that according to Eq. (B4)

$$\tau_1 = \frac{s_1}{s_1 + s_2} \tau. \quad (\text{B8})$$

After the parameters of $S^{(1)}(r)$ are determined its analytical form is derived from Eqs. (12) and (16) and subtracted from $S_2(r)$ to obtain $S_2^{(2)}(r)$, which is also parameterized using the single-

mode method. For each value of the parameter α the tightness of the fit in the lag range $[0, L_e]$ of the measured structure function $S_2(r)$ by the corresponding analytical form $S_2^{(1)}(r) + S_2^{(2)}(r)$ is evaluated, and the value of α is determined by the best fit.

Figure B1 illustrates the above fitting method on the example of the data from the Indian Ocean, which is also presented in Fig. 6(e). The red curve corresponds to the SF derived from the data. The partial saturation is clearly seen at the scales below 400 km. The initial single-mode fit based on the variance observed in the sample is shown by the dashed blue curve. The discrepancy between the measured SF and the fit are evident, since the SF exhibits large-scale behavior inconsistent with the local variance s^2 (the asymptote $2s^2$ of the fitting curve is shown by the horizontal dashed line). The 2-mode fit assuming the same variance s^2 is depicted by solid blue curve, while its trend and MBL components are represented in respectively orange and green. This fit also significantly deviates from the measured SF at scales larger than 400 km, however, it closely captures the SF's shape at smaller scales allowing us to single out the MBL component's SF and to split the total AOT into within- and above-MBL parts.

References

- Alexandrov, M. D., A. Marshak, B. Cairns, A. A. Lacis, and B. E. Carlson, 2004: Scaling properties of aerosol optical thickness retrieved from ground-based measurements. *J. Atmos. Sci.*, **61**, 1024–1039.
- Anderson, T. L., R. J. Charlson, D. M. Winker, J. A. Ogren, and K. Holmen, 2003: Mesoscale variations of tropospheric aerosols. *J. Atmos. Sci.*, **60**, 119–136.
- Bell, T. L., 1987: A space-time stochastic model of rainfall for satellite remote-sensing studies. *J. Geophys. Res.*, **92D**, 9631–9643.

603 Benedetti, A., and Coauthors, 2009: Aerosol analysis and forecast in the European Centre for
604 Medium-Range Weather Forecasts Integrated Forecast System: 2. data assimilation. *J. Geophys.*
605 *Res.*, **114**, D13 205.

606 Cahalan, R. F., and J. B. Snider, 1989: Marine stratocumulus structure during FIRE. *Remote Sens.*
607 *Environ.*, **28**, 95–107.

608 Curran, P. J., 1988: The semivariogram in remote sensing: An introduction. *Remote Sens. Environ.*,
609 **24**, 493–507.

610 Davis, A., A. Marshak, R. Cahalan, and W. Wiscombe, 1997: The landsat scale-break in stratocu-
611 mulus as a three-dimensional radiative transfer effect, implications for cloud remote sensing. *J.*
612 *Atmos. Sci.*, **54**, 241–260.

613 Davis, A., A. Marshak, H. Gerber, and W. Wiscombe, 1999: Horizontal structure of marine
614 boundary-layer clouds from cm- to km-scales. *J. Geophys. Res.*, **104**, 6123–6144.

615 Davis, A., A. Marshak, W. Wiscombe, and R. Cahalan, 1994: Multifractal characterizations of
616 nonstationarity and intermittency in geophysical fields: Observed, retrieved, or simulated. *J.*
617 *Geophys. Res.*, **99**, 8055–8072.

618 Davis, A., A. Marshak, W. Wiscombe, and R. Cahalan, 1996: Scale invariance of liquid water dis-
619 tributions in marine stratocumulus. Part I: Spectral properties and stationarity issues. *J. Atmos.*
620 *Sci.*, **53**, 1538–1558.

621 Gage, K. S., and G. D. Nastrom, 1986: Theoretical interpretation of atmospheric wavenumber
622 spectra of wind and temperature observed by commercial aircraft during GASP. *J. Atmos. Sci.*,
623 **43**, 729–740.

624 Geogdzhayev, I., B. Cairns, M. Mishchenko, K. Tsigaridis, and T. van Noije, 2014: Model-based
 625 estimation of sampling-caused uncertainty in aerosol remote sensing for climate research appli-
 626 cations. *Q. J. R. Meteorol. Soc.*, **140**, 2353–2363.

627 Hansen, J., M. Sato, R. Ruedy, A. Lacis, and V. Oinas, 2000: Global warming in the twenty-first
 628 century: An alternative scenario. *Proc. Natl. Acad. Sci.*, **97**, 9875–9880.

629 Huneeus, N., and Coauthors, 2011: Global dust model intercomparison in AeroCom phase I.
 630 *Atmos. Chem. Phys.*, **11**, 7781–7816.

631 Kinne, S., and Coauthors, 2006: An aerocom initial assessment optical properties in aerosol
 632 component modules of global models. *Atmos. Chem. Phys.*, **6**, 1815–1834.

633 Koch, D., T. C. Bond, D. Streets, N. Unger, and G. R. van der Werf, 2007: Global impacts of
 634 aerosols from particular source regions and sectors. *J. Geophys. Res.*, **112**, D02 205.

635 Kolmogorov, A. N., 1941: Local structure of turbulence in an incompressible liquid for very large
 636 Reynolds numbers. *Dokl. Akad. Nauk SSSR*, **30**, 299–303.

637 Levy, R. C., L. A. Remer, R. G. Kleidman, S. Mattoo, C. Ichoku, R. Kahn, and T. F. Eck, 2010:
 638 Global evaluation of the Collection 5 MODIS dark-target aerosol products over land. *Atmos.*
 639 *Chem. Phys.*, **10**, 10 399–10 420.

640 Lilly, D., 1989: Two-dimensional turbulence generated by energy sources at two scales. *J. Atmos.*
 641 *Sci.*, **46**, 2026–2030.

642 Lovejoy, S., and D. Schertzer, 2010: Towards a new synthesis for atmospheric dynamics: Space-
 643 time cascades. *Atmos. Res.*, **96**, 1–52.

644 Lovejoy, S., and D. Schertzer, 2012: Haar wavelets, fluctuations and structure functions: conve-
 645 nient choices for geophysics. *Nonlinear Processes in Geophysics*, **19**, 513–527.

- 646 Mandelbrot, B. B., 1982: *The Fractal Geometry of Nature*. W. H. Freeman, 460 pp.
- 647 Marshak, A., A. Davis, W. Wiscombe, and R. Cahalan, 1997: Scale-invariance of liquid water
648 distributions in marine stratocumulus, Part 2 – Multifractal properties and intermittency issues.
649 *J. Atmos. Sci.*, **54**, 1423–1444.
- 650 Mejia, J. M., and I. Rodriguez-Iturbe, 1974: Correlation links between normal and log normal
651 processes. *Water Resour. Res.*, **10**, 689–690.
- 652 Morcrette, J.-J., and Coauthors, 2009: Aerosol analysis and forecast in the European Centre for
653 Medium-Range Weather Forecasts Integrated Forecast System: Forward modeling. *J. Geophys.*
654 *Res.*, **114**, D06 206.
- 655 Myhre, G., and Coauthors, 2013: Radiative forcing of the direct aerosol effect from aerocom phase
656 ii simulations. *Atmos. Chem. Phys.*, **13** (4), 1853–1877.
- 657 O’Neill, N. T., A. Ignatov, B. N. Holben, and T. F. Eck, 2000: The lognormal distribution as a
658 reference for reporting aerosol optical depth statistics; Empirical tests using multi-year, multi-
659 site AERONET sunphotometer data. *Geophys. Res. Lett.*, **27**, 3333–3336.
- 660 Quaas, J., and Coauthors, 2009: Aerosol indirect effects – general circulation model intercompar-
661 ison and evaluation with satellite data. *Atmos. Chem. Phys.*, **9** (22), 8697–8717.
- 662 Redemann, J., M. A. Vaughan, Q. Zhang, Y. Shinozuka, P. B. Russell, J. M. Livingston,
663 M. Kacenelenbogen, and L. A. Remer, 2012: The comparison of MODIS-Aqua (C5) and
664 CALIOP (V2&V3) aerosol optical depth. *Atmos. Chem. Phys.*, **12**, 3025–3043.
- 665 Remer, L. A., and Coauthors, 2005: The MODIS aerosol algorithm, products and validation. *J.*
666 *Atmos. Sci.*, **62**, 947–973.

667 Remer, L. A., and Coauthors, 2008: Global aerosol climatology from the MODIS satellite sensors.
668 *J. Geophys. Res.*, **113**, D14S07.

669 Schmidt, G. A., and Coauthors, 2014: Configuration and assessment of the GISS modelE2 contri-
670 butions to the CMIP5 archive. *J. Adv. Model. Earth Syst.*, **6**, 141–184.

671 Takemura, T., T. Nozawa, S. Emori, T. Y. Nakajima, and T. Nakajima, 2005: Simulation of cli-
672 mate response to aerosol direct and indirect effects with aerosol transport-radiation model. *J.*
673 *Geophys. Res.*, **110**, D02 202.

674 Takemura, T., H. Okamoto, Y. Maruyama, A. Numaguti, A. Higurashi, and T. Nakajima, 2000:
675 Global three-dimensional simulation of aerosol optical thickness distribution of various origins.
676 *J. Geophys. Res.*, **105**, 17 853–17 873.

677 Unger, N., D. T. Shindell, D. M. Koch, and D. G. Streets, 2008: Air pollution radiative forcing
678 from specific emissions sectors at 2030. *J. Geophys. Res.*, **113**, D02 306.

679 Winker, D. M., M. A. Vaughan, A. H. Omar, Y. Hu, K. A. Powell, Z. Liu, W. H. Hunt, and S. A.
680 Young, 2009: Overview of the CALIPSO mission and CALIOP data processing algorithms. *J.*
681 *Atmos. Oceanic Technol.*, **26**, 2310–2323.

682 Winker, D. M., and Coauthors, 2010: The CALIPSO Mission: A global 3d view of aerosols and
683 clouds. *Bull. Am. Meteorol. Soc.*, **91**, 1211–1229.

684 Yao, M.-S., and Y. Cheng, 2012: Cloud simulations in response to turbulence parameterizations
685 in the giss model e gcm. *J. Climate*, **25**, 4963–4974.

LIST OF FIGURES

- Fig. 1.** Dependence of the normalized structure function $S_2(r)/2s^2$ shape (Eqs. (12), (16)) on the parameters $v = s/\bar{\tau}$ (top), L_e (middle), and H (bottom). 36
- Fig. 2.** Two regions of different scales, MODIS data from which were used for computation of structure functions presented in Fig. 3. 37
- Fig. 3.** Structure functions computed from MODIS data over South Pacific Ocean obtained on January 17, 2006. Top left: SF (red) for large $120^\circ \times 70^\circ$ area exhibiting statistical saturation at large scales. Blue curve represents the parametric fit to the data. Top right: the same SF as in the top left panel (red) but for shorter scale range in comparison with local SF (green) from a $10^\circ \times 10^\circ$ area. Maps presenting MODIS pixels used for SF computations are included in both plots as inserts. Bottom left: Fit to the local SF using locally measured standard deviation. Bottom right: Same as at bottom left but when the large-scale value (from top left plot) of the standard deviation is assumed. 38
- Fig. 4.** Structure function from Fig. 3 (green) and number of MODIS pixel pairs N_p contributed to the SF value at each lag (black). The lag interval with admissible number of pairs (more than 1800) is indicated by the horizontal blue line. The two orange curves corresponding to $S_2 \pm \text{const} \cdot N_p^{-1/2}$ illustrate the growth of SF computation uncertainty with the decline of N_p 39
- Fig. 5.** Schematic representation of the partial saturation feature seen in structure functions from Figs. 6 and 3 as a sum of stationary and trend components. 40
- Fig. 6.** Structure functions computed using MODIS data from various $10^\circ \times 10^\circ$ ocean regions (shown in top left plot) obtained on August 18, 2006: (a) relatively pristine Pacific Ocean unaffected by long-range aerosol transport; (b) African coastal waters with strong presence of Saharan dust; (c) area off-coast of equatorial Africa affected by biomass burning smoke; (d) northern Indian Ocean with presence of dust from Arabian Peninsula; and (e) middle of the Indian Ocean, data from which still shows presence of the transported aerosol. In all plots the red curve corresponds to the SF derived from the data, while the fits obtained from single-mode and 2-mode models are shown by respectively solid and dashed blue lines. The SFs and parameters of the stationary MBL AOT component are shown in green. Maps showing the actual MODIS pixels used for SF computations are included in each plot as inserts. 41
- Fig. 7.** Monthly averages of MODIS retrievals from August 2006: mean AOT (top), its standard deviation (middle), and the ratio of the standard deviation and the mean (bottom). 42
- Fig. 8.** Same as in Fig. 7 but for retrieved structure function parameters of single-component model: L_e (top) and H (bottom). 43
- Fig. 9.** Maps of monthly averages from GISS GCM output: total AOT (top) and MBL height (bottom). The simulations are for August 2006. 44
- Fig. 10.** Maps (for August 2006) of monthly averaged AOTs of transported (above-MBL, top) and MBL (bottom) components from MODIS structure function analysis (left) and from GISS GCM output (right). The data presented in left panels have been enhanced for comparison with GCM: interpolated to $2.5^\circ \times 2.5^\circ$ grid and smoothed by moving averaging. Note that monthly averages for each mode were taken only over days when this mode was present, thus, the components means do not add up to the total mean in Fig. 7 (top). 45

728 **Fig. 11.** Same as Fig. 10 but for the fractions of the above-MBL AOT in the total one. The color bars
729 in the left (MODIS) and right (GCM) plots are chosen different for better comparison of the
730 geographical features. 46

731 **Fig. B1.** Details of structure function fitting method. The data is from the middle of Indian Ocean also
732 presented in Fig. 6(e). The red curve corresponds to the SF derived from the data, while the
733 fits obtained from single-mode and 2-mode models are shown by respectively dashed and
734 solid blue lines. The SFs for the trend and stationary (boundary layer) AOT components
735 from 2-mode retrievals are shown by respectively orange and green curves. 47

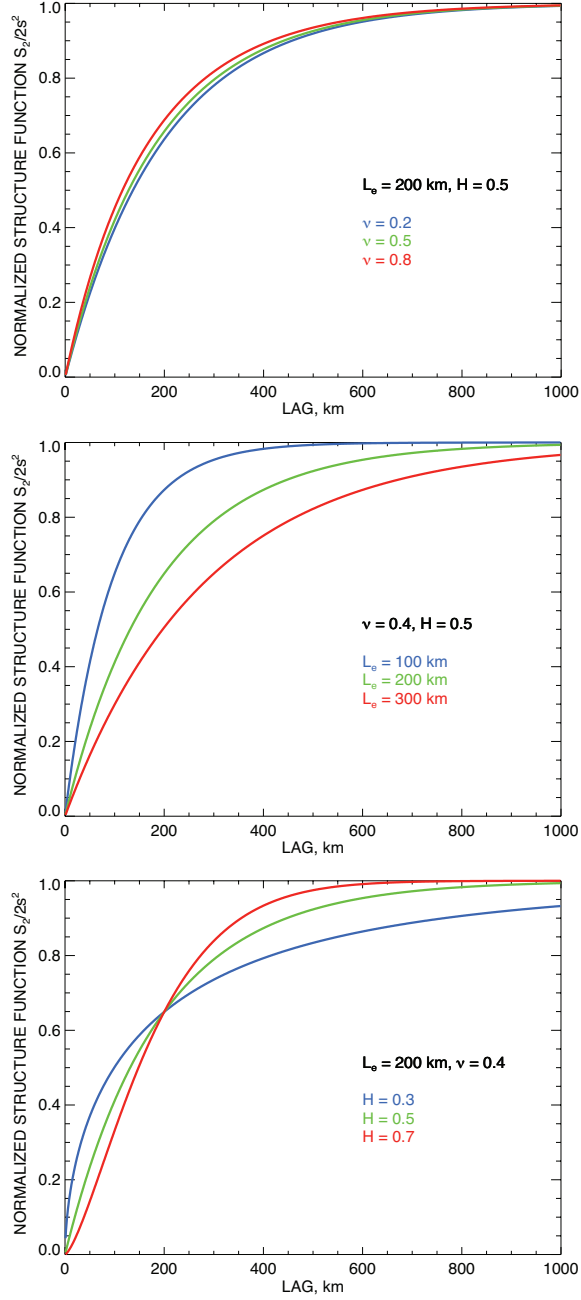
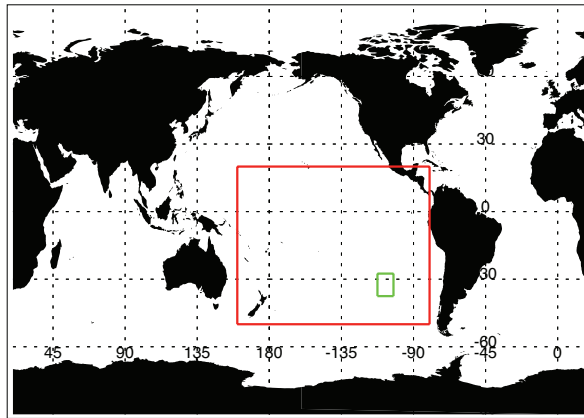


FIG. 1. Dependence of the normalized structure function $S_2(r)/2s^2$ shape (Eqs. (12), (16)) on the parameters $\nu = s/\bar{\tau}$ (top), L_e (middle), and H (bottom).



738 FIG. 2. Two regions of different scales, MODIS data from which were used for computation of structure
 739 functions presented in Fig. 3.

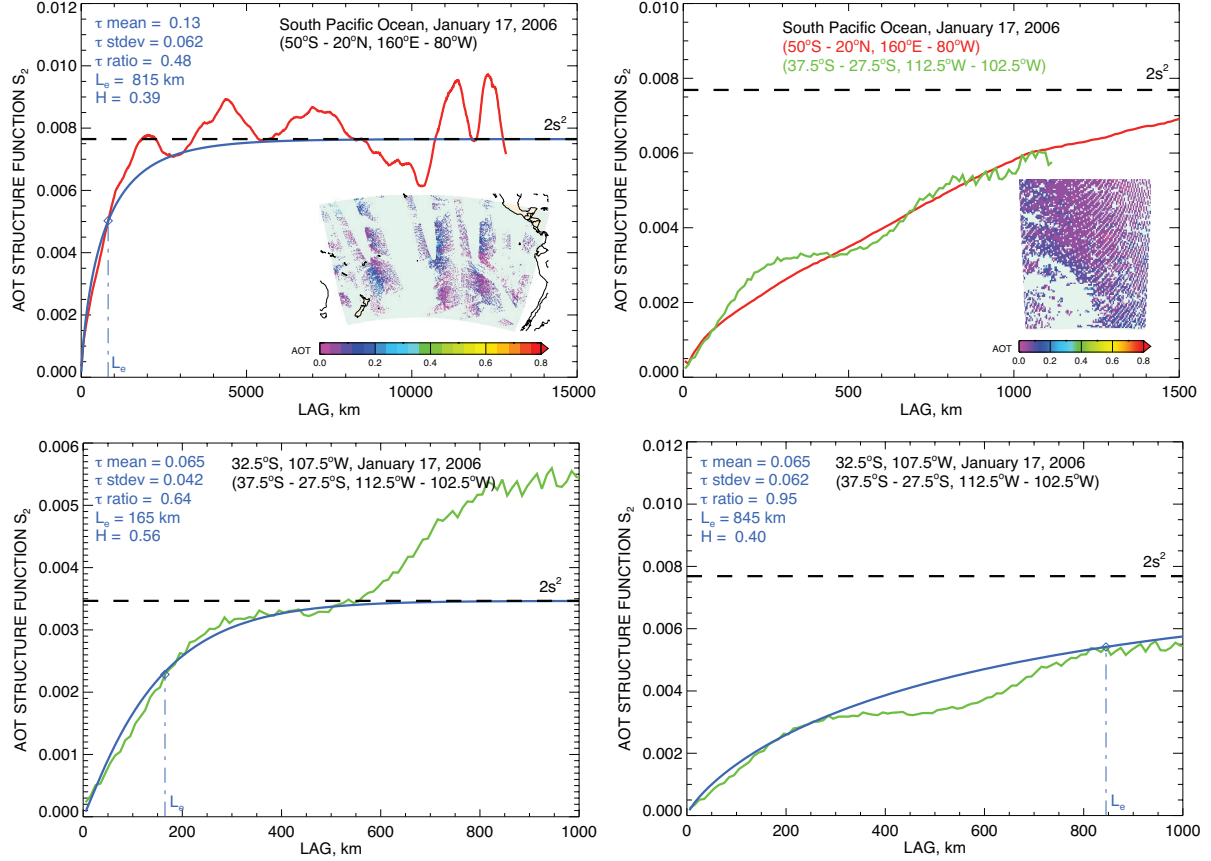
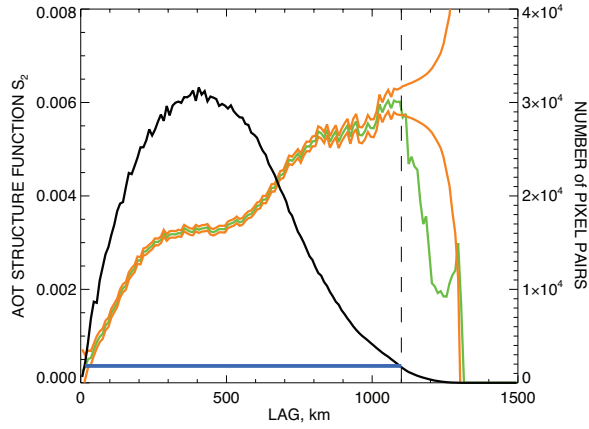
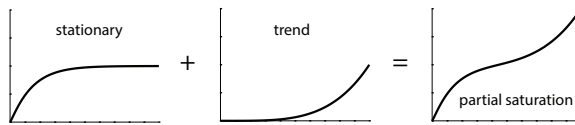


FIG. 3. Structure functions computed from MODIS data over South Pacific Ocean obtained on January 17, 2006. Top left: SF (red) for large $120^\circ \times 70^\circ$ area exhibiting statistical saturation at large scales. Blue curve represents the parametric fit to the data. Top right: the same SF as in the top left panel (red) but for shorter scale range in comparison with local SF (green) from a $10^\circ \times 10^\circ$ area. Maps presenting MODIS pixels used for SF computations are included in both plots as inserts. Bottom left: Fit to the local SF using locally measured standard deviation. Bottom right: Same as at bottom left but when the large-scale value (from top left plot) of the standard deviation is assumed.



747 FIG. 4. Structure function from Fig. 3 (green) and number of MODIS pixel pairs N_p contributed to the SF
 748 value at each lag (black). The lag interval with admissible number of pairs (more than 1800) is indicated by
 749 the horizontal blue line. The two orange curves corresponding to $S_2 \pm \text{const} \cdot N_p^{-1/2}$ illustrate the growth of SF
 750 computation uncertainty with the decline of N_p .



751 FIG. 5. Schematic representation of the partial saturation feature seen in structure functions from Figs. 6 and
 752 3 as a sum of stationary and trend components.

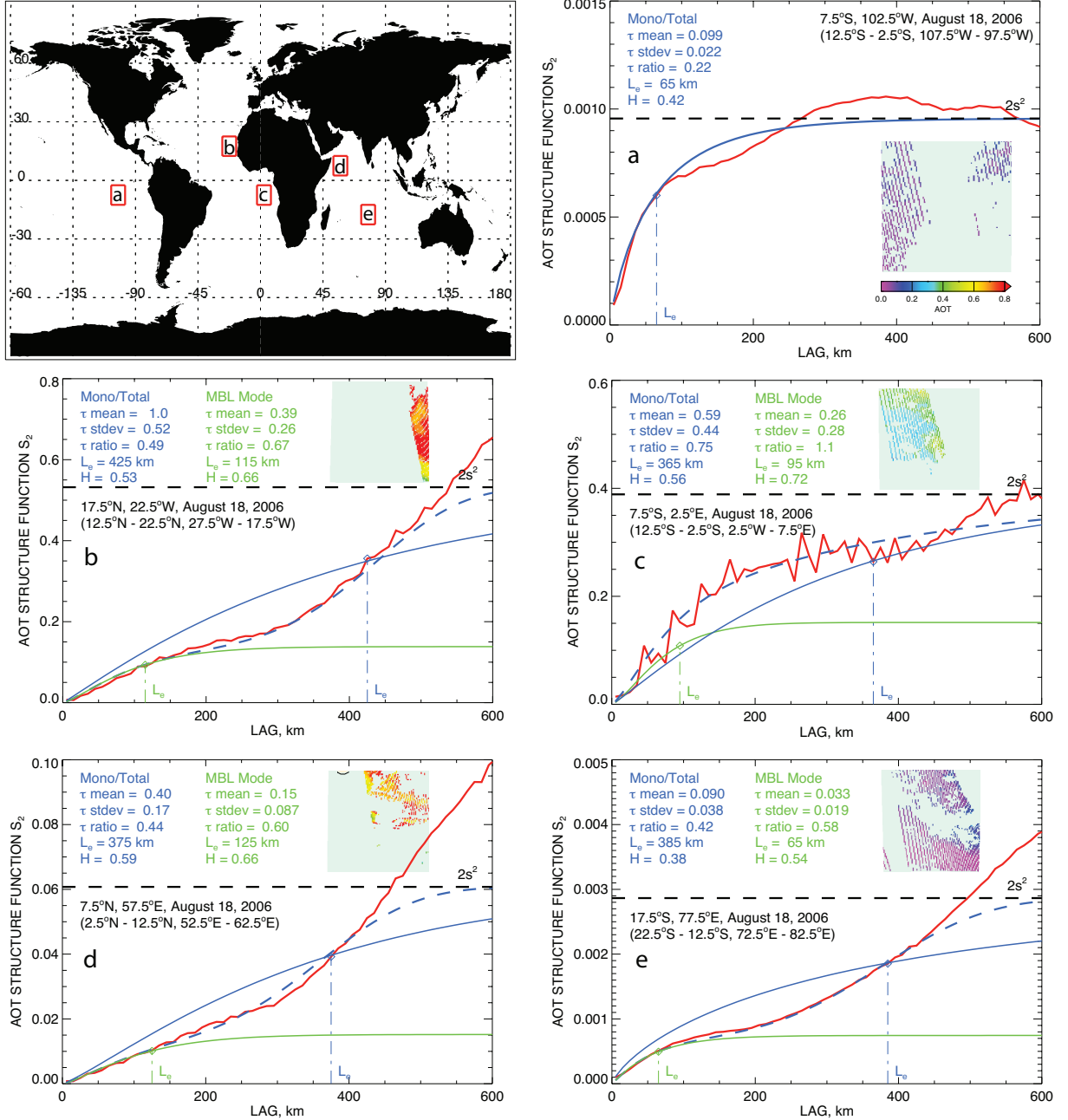


FIG. 6. Structure functions computed using MODIS data from various $10^\circ \times 10^\circ$ ocean regions (shown in top left plot) obtained on August 18, 2006: (a) relatively pristine Pacific Ocean unaffected by long-range aerosol transport; (b) African coastal waters with strong presence of Saharan dust; (c) area off-coast of equatorial Africa affected by biomass burning smoke; (d) northern Indian Ocean with presence of dust from Arabian Peninsula; and (e) middle of the Indian Ocean, data from which still shows presence of the transported aerosol. In all plots the red curve corresponds to the SF derived from the data, while the fits obtained from single-mode and 2-mode models are shown by respectively solid and dashed blue lines. The SFs and parameters of the stationary MBL AOT component are shown in green. Maps showing the actual MODIS pixels used for SF computations are included in each plot as inserts.

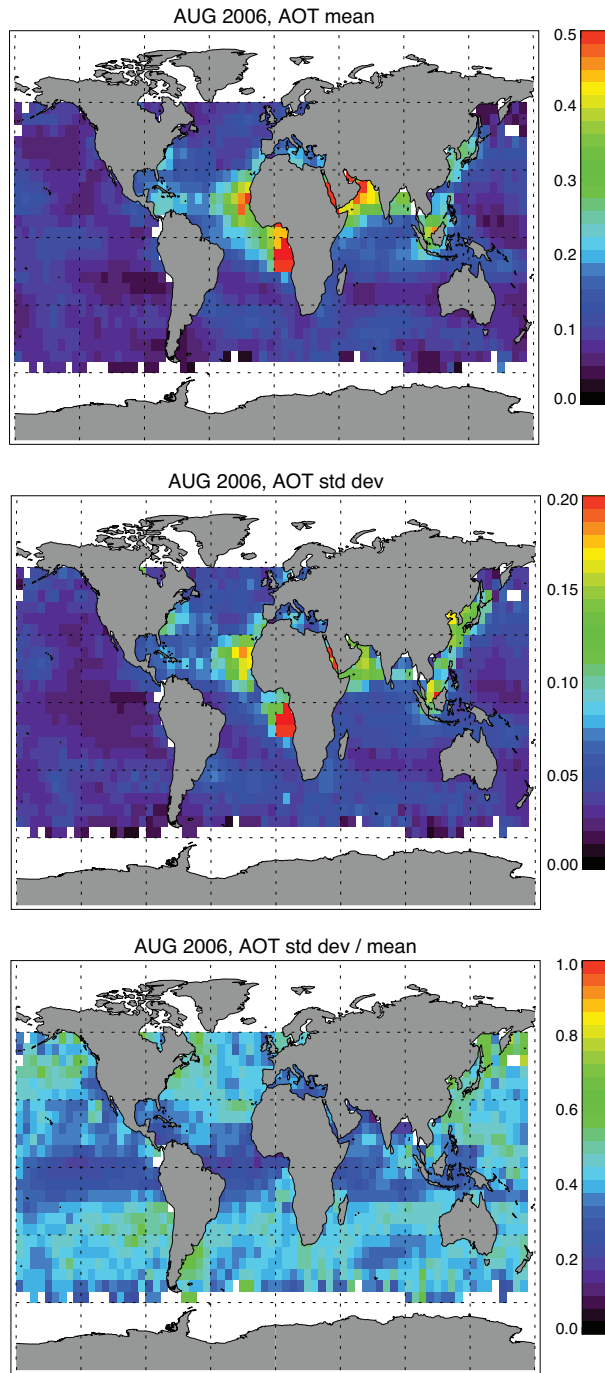


FIG. 7. Monthly averages of MODIS retrievals from August 2006: mean AOT (top), its standard deviation (middle), and the ratio of the standard deviation and the mean (bottom).

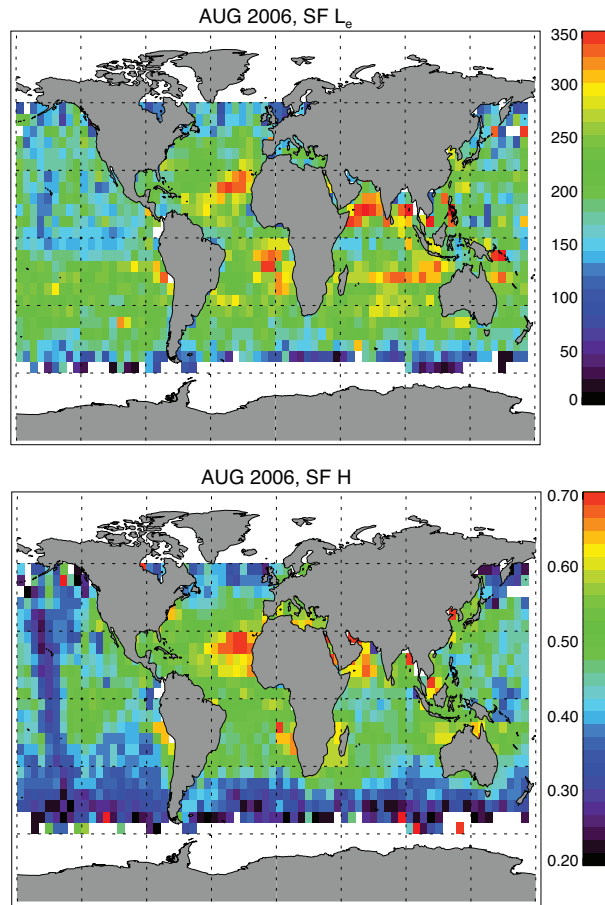
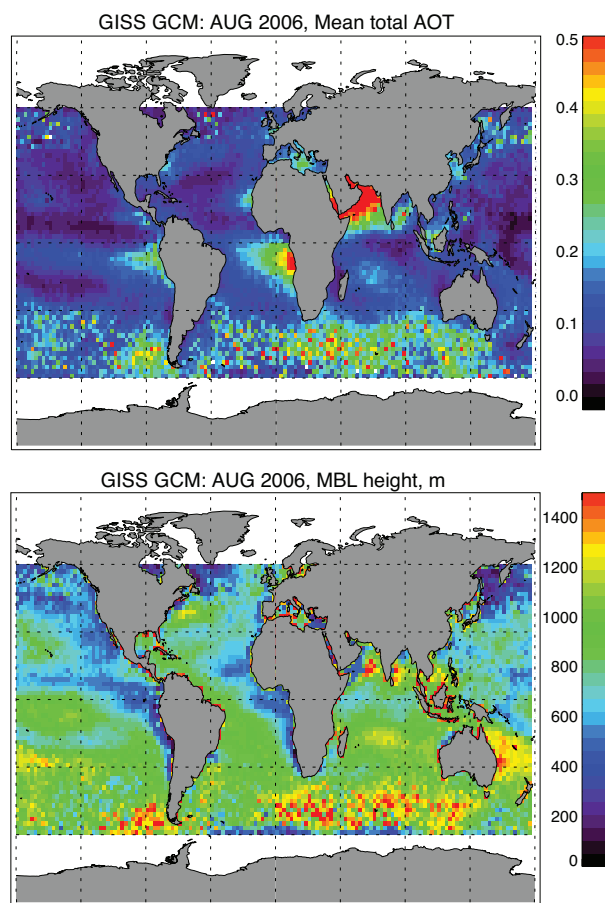
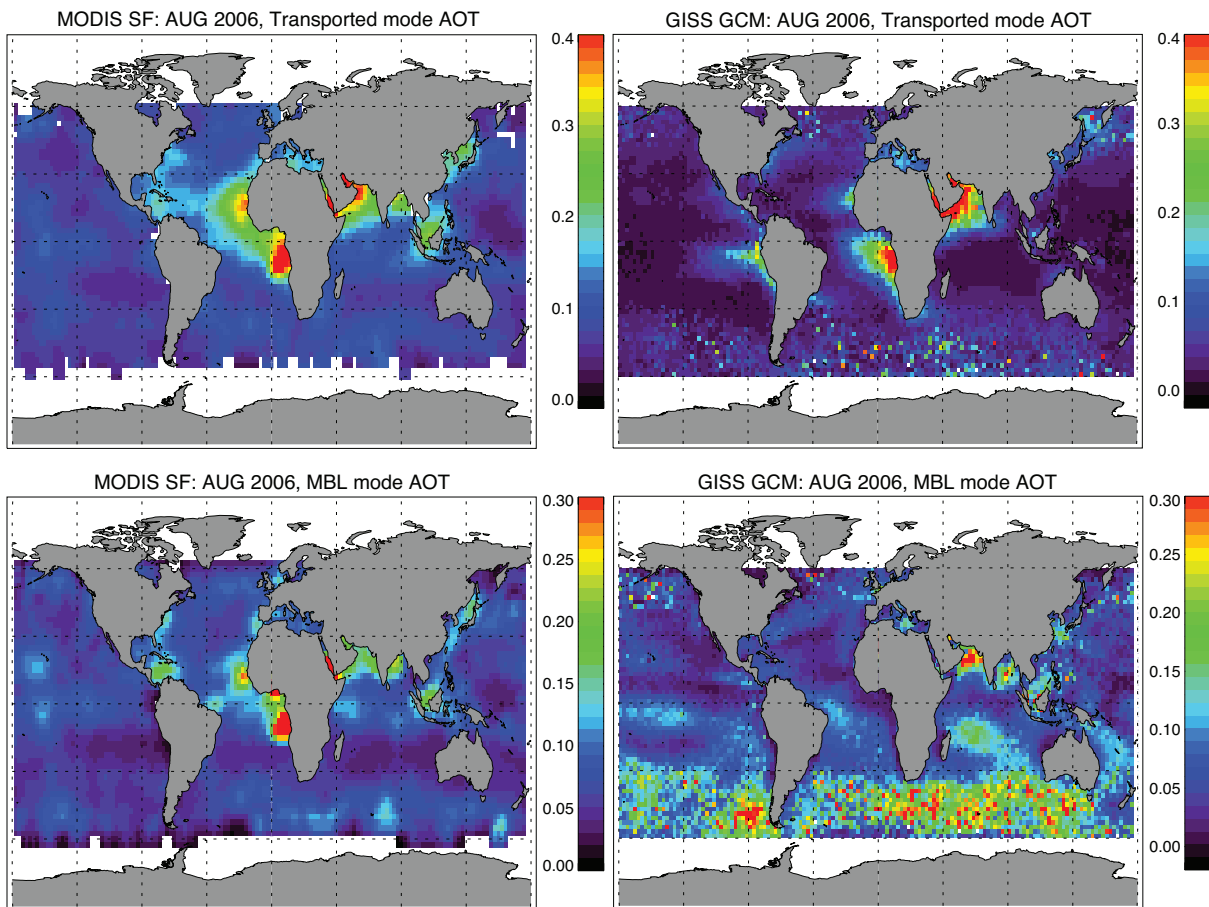


FIG. 8. Same as in Fig. 7 but for retrieved structure function parameters of single-component model: L_e (top) and H (bottom).

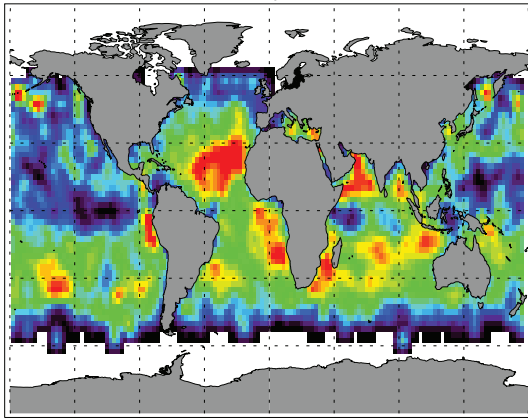


766 FIG. 9. Maps of monthly averages from GISS GCM output: total AOT (top) and MBL height (bottom). The
 767 simulations are for August 2006.

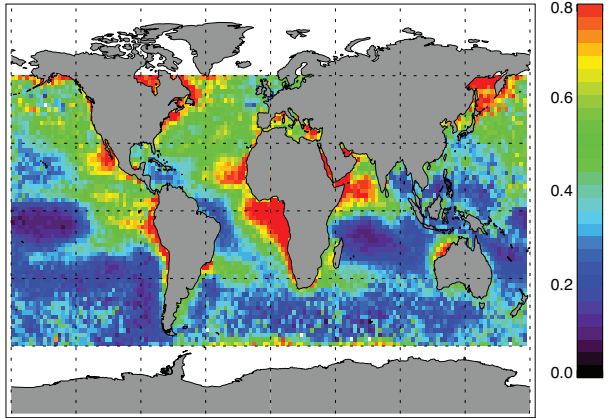


768 FIG. 10. Maps (for August 2006) of monthly averaged AOTs of transported (above-MBL, top) and MBL
 769 (bottom) components from MODIS structure function analysis (left) and from GISS GCM output (right). The
 770 data presented in left panels have been enhanced for comparison with GCM: interpolated to $2.5^\circ \times 2.5^\circ$ grid and
 771 smoothed by moving averaging. Note that monthly averages for each mode were taken only over days when this
 772 mode was present, thus, the components means do not add up to the total mean in Fig. 7 (top).

MODIS SF: AUG 2006, Transported mode fraction in AOT



GISS GCM: AUG 2006, Transported mode fraction in AOT



773 FIG. 11. Same as Fig. 10 but for the fractions of the above-MBL AOT in the total one. The color bars in the
774 left (MODIS) and right (GCM) plots are chosen different for better comparison of the geographical features.

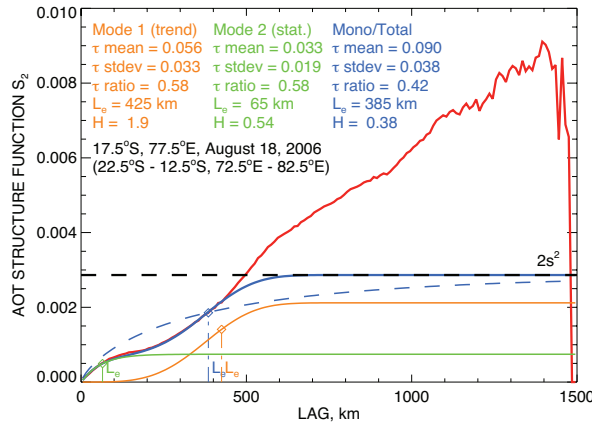


Fig. B1. Details of structure function fitting method. The data is from the middle of Indian Ocean also presented in Fig. 6(e). The red curve corresponds to the SF derived from the data, while the fits obtained from single-mode and 2-mode models are shown by respectively dashed and solid blue lines. The SFs for the trend and stationary (boundary layer) AOT components from 2-mode retrievals are shown by respectively orange and green curves.

Supplemental Material

[Click here to download Supplemental Material: alexandrov_sup.pdf](#)